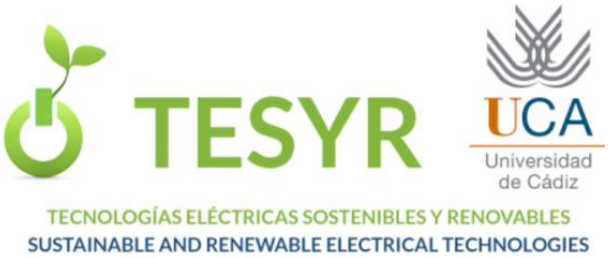

Universidad de Cádiz

Experimental study of distributed control for renewable energy/energy storage/hydrogen system-based microgrid clustes using Raspberry Pi agents

Carrasco González, David; Sarrias Mena, Raúl; Horrillo Quintero, Pablo; Hosseini, Ehsan; Llorens Iborra, Francisco; Fernández Ramírez, Luis Miguel

Published in:
Electric Power Systems Research

DOI (link to publication from Publisher):
10.1016/j.epsr.2026.113249

Publication date:
2026

Document Version:
Published

Citation for published version (IEEE):
D. Carrasco-González, R. Sarrias-Mena, P. Horrillo-Quintero, E. Hosseini, F. Llorens-Iborra, and L. M. Fernández-Ramírez, "Experimental study of distributed control for renewable energy/energy storage/hydrogen system-based microgrid clusters using Raspberry Pi agents," Electric Power Systems Research, vol. 259, p. 113249, Oct. 2026, doi: 10.1016/J.EPSR.2026.113249.

Electric Power Systems Research 259 (2026) 113249

Contents lists available at ScienceDirect

Electric Power Systems Research

journal homepage: www.elsevier.com/locate/epsr

Experimental study of distributed control for renewable energy/energy storage/hydrogen system-based microgrid clusters using Raspberry Pi agents

David Carrasco-González [a], Raúl Sarrias-Mena [b], Pablo Horrillo-Quintero [c], Ehsan Hosseini [a], Francisco Llorens-Iborra [a], Luis M. Fernández-Ramírez [a,*]

[a] Research Group in Sustainable and Renewable Electrical Technologies - SURET (PAIDI-TEP-023), Department of Electrical Engineering, University of Cadiz, Higher Technical School of Engineering of Algeciras (ETSIA), Avda. Ramón Puyol, s/n, 11202, Algeciras, Cadiz, Spain
[b] SURET (PAIDI-TEP-023), Department of Engineering in Automation, Electronics and Computer Architecture & Networks, University of Cadiz, ETSIA, Avda. Ramón Puyol, s/n, 11202, Algeciras, Cadiz, Spain
[c] SURET (PAIDI-TEP-023), Department of Electrical Engineering, University of Cadiz, ESI Puerto Real, Avda. Universidad de Cádiz, n° 10, 11519 Puerto Real, Cadiz, Spain

ARTICLE INFO

Keywords:
Control agents
Distributed control
Microgrids cluster
Real-time control
Energy storage systems
Renewable energy

ABSTRACT

Microgrid clusters (MGCs) are emerging as a promising solution for integrating diverse DC and AC technologies, thereby enhancing flexibility and resilience. This research presents an experimental study of a control strategy for a MGC comprising two microgrids (MGs), interconnected with each other: a DC MG with a wind generator, an ultracapacitor, DC local loads, and a hydrogen system; and an AC MG that includes an electric battery, AC local loads, and a photovoltaic power plant. Through experimental validation, this research produces valuable findings into the design and implementation of advanced MGC technologies. The proposed control strategy leverages local controllers and a distributed control architecture that includes two control agents, which coordinates the power management between the technologies of the MGC. The experimental setup, consisting of an OPAL-RT unit and two Raspberry Pi boards, is implemented for the real-time testing and verification of the control methodology across a range of operational scenarios. The real-time experimental results validate the effectiveness of the proposed control methodology. Additionally, the control strategy exhibits superior integral time absolute error performance compared to a centralized control architecture. Finally, a study on communication delays across all control agents reveals that while performance degrades, system stability is maintained.

1. Introduction

Currently, driven by the global decarbonization of energy systems and the increasing global demand for energy, microgrids (MGs) have emerged as autonomous entities that integrate local electrical loads, energy storage systems (ESSs), and renewable energy sources. MGs offer numerous benefits, including superior energy performance, reduced harmful environmental emissions, better power quality and reliability, and a more economical operation [1]. While research initially concentrated AC configurations owing to existing conventional infrastructure, DC and hybrid MGs are gaining prominence for their superior adaptability to diverse operational configurations [2,3].

Concerning their connection to an external grid, MGs can operate in two modes: standalone or grid-connected. Standalone MGs, typical in remote locations such as islands [4], operate independently without external grid support. Grid-connected MGs, on the other hand, are operated in conjunction with a grid, compensating for the power imbalances within the MG [5]. In this situation, the MGs can also operate in standalone mode [6]. In the standalone mode, energy produced within the MG must either be stored in ESSs for future usage or consumed by the loads, due to the lack of connection to the local grid [7].

The coordination and interconnection of several multiple nearby MGs forms a microgrid cluster (MGC) [8], which offers different benefits, like: 1) advancing the decentralization of power systems by reducing the reliance on traditional grids and encouraging local energy independence; 2) facilitating the integration of different components

* Corresponding author.
E-mail addresses: david.carrasco@uca.es (D. Carrasco-González), raul.sarrias@uca.es (R. Sarrias-Mena), pablo.horrillo@uca.es (P. Horrillo-Quintero), ehsan.hosseini@uca.es (E. Hosseini), francisco.llorens@uca.es (F. Llorens-Iborra), luis.fernandez@uca.es (L.M. Fernández-Ramírez).

https://doi.org/10.1016/j.epsr.2026.113249
Received 13 January 2026; Received in revised form 26 April 2026; Accepted 30 April 2026
Available online 2 May 2026

within individual MGs and across the whole cluster; 3) enhancing sustainability, reliability, efficiency and resilience compared to individual MGs; and 4) promoting the local electricity production and consumption, thereby enhancing grid stability and self-sufficiency [9].

Various architectural approaches are employed to achieve specific objectives in the MGC control [10–12]. In [11], the researchers proposed a stationary centralized control agent for an AC MG. Researchers in [12] developed a hierarchical control agent for an AC MG. One of these approaches is the distributed architecture, where control agents are employed to achieve goals and coordinate the behavior of the systems. Each control agent leverages data shared by adjacent agents and information collected from the MGs. These control agents provide reference signals to the different technologies, which can be determined through various methods [13].

The growing interest in MGs requires the development of sophisticated distributed control agents to tackle the opportunities and challenges presented by these systems [14]. However, most existing works have focused on using distributed control for secondary control in the MGs and MGCs, which involves voltage and frequency regulation in the MGs [15,16]. Researchers in [15] developed the secondary control for a determined island AC MG; and the control designed in [16] was developed for another islanded AC MG. In power distribution, distributed control has been explored within individual MGs [17–19]. In [17], the authors developed the distributed EMS for a grid-connected residential AC MG; and in [18], the distributed EMS was used for an islanded AC MG. Researchers in [19] developed a distributed economic dispatch for an islanded AC MG with the participation of thermostatically controlled loads.

In some cases, authors use the term “distributed control” for power distribution in MGC [20,21], while these are hierarchical controls, with one control agent per MG and a central control agent that monitors and manages the system. Additionally, these controls were studied in DC MGCs. In the case of the application of distributed control agents for power distribution in MGCs, reference [22] examined this type of control in an islanded MGC but lacked experimental validation, while reference [23] investigated it in a MGC without a hydrogen system. The latter study tested the control approach over long time horizons, relying on historical data and databases without dynamically adapting to real-time changes, and it also lacked experimental validation. In [24], a distributed control agent architecture was applied to a MGC. However, this system operated in standalone mode and only tested the control approach over long time horizons without experimental validation. Finally, a distributed control agent architecture was applied to a grid-connected MGC in [25], but this work also lacked experimental validation and was tested over long-time horizons.

While theoretical analysis is valuable, verifying the practical performance of MG control systems needs experimental testing. These experiments must prioritize flexibility, ease of implementation, security, cost-effectiveness, and accuracy. To address these challenges, researchers have introduced innovative validation techniques [26]. Among all the options available, the combination of an OPAL-RT unit and Raspberry Pi (RPi) boards offer a scalable, customizable, and cost-effective hardware-in-the-loop (HIL) setup that facilitates rapid control prototyping and deployment.

Table 1 provides a comparative study of existing literature on control agents for MGs/MGCs, contrasting them with the novel control methodology implemented in this research. As shown in Table 1, this research develops the implementation and HIL verification of a novel control methodology for a grid-connected DC/AC MGC comprising two different MGs. The control methodology leverages a distributed control architecture and local controllers, where the distributed architecture employs two different control agents to coordinate the power management between the technologies used in the system. This control strategy is introduced and validated in a HIL setup utilizing two RPi boards and an OPAL-RT unit.

As conclusions from Table 1, this research produces several key findings, which are outlined below:

- Development of a novel dynamic control strategy for a MGC that integrates both AC and DC MGs. The system incorporates a diverse range of components, including solar photovoltaic (PV) and wind turbines as renewable sources, battery ESSs (BESS), fuel cell (FC), ultracapacitor (UC) and electrolyzer (EZ) as storage devices, and both DC and AC loads.
- Development of a dynamic distributed control architecture, comprising two control agents, one for each MG. These control agents dynamically distribute power references among the ESSs within their respective MG and exchange information with the control agent of the other MG.
- Implementation of a comprehensive experimental configuration, based on an OPAL-RT 4512 real-time unit, two RPi 4B boards and a

Table 1
Comparative study of the existing works about control agents in MGs/MGCs.

(a) Paper	[11]	[12]	[13]	[15]	[16]	[17]	[18]	[19]
Dynamic Control	-	-	-	✓	✓	✓	✓	✓
Detailed Models	-	✓	-	-	-	-	-	✓
BESS/ Hydrogen/UC	-	-	-	-	-	-	-	-
DC-AC MGC	-	-	-	-	-	-	-	-
Grid-connected	✓	✓	✓	-	-	✓	-	-
Distributed Control Strategy	-	-	✓	✓	✓	✓	✓	✓
Distributed Power Sharing	-	-	✓	-	-	✓	✓	✓
Experimental Validation	-	✓	-	✓	-	-	-	-
RPi Validation per Agent	-	-	-	-	-	-	-	-
Latencies Study	-	-	-	-	-	-	-	-

(b) **Paper**	[20]	[21]	[22]	[23]	[24]	[25]	**Paper**
Dynamic Control	✓	✓	✓	-	-	-	✓
Detailed Models	-	-	-	-	-	-	✓
BESS/ Hydrogen/UC	-	-	-	-	-	-	✓
DC-AC MGC	-	-	-	-	-	-	✓
Grid-connected	-	✓	-	✓	-	✓	✓
Distributed Control Strategy	-	-	✓	✓	✓	✓	✓
Distributed Power Sharing	-	-	✓	✓	✓	✓	✓
Experimental Validation	✓	✓	-	-	-	-	✓
RPi Validation per Agent	-	-	-	-	-	-	✓
Latencies Study	✓	✓	-	-	-	-	✓

host PC, integrated in a communication network. This setup enables realistic testing and validation of the system performance.

- Design of the control methodology to handle a wide selection of operating conditions, including variable wind speed, solar radiation and load fluctuations, ensuring robust and efficient operation.
- Demonstration of the effectiveness of the proposed dynamic distributed control architecture, which achieves superior Integral Time Absolute Error (ITAE) performance for the ESS management and the DC bus voltage control compared to a centralized control architecture.
- Comprehensive study of the impact on the system performance of different degrees of standard communication latencies in all the control agents.

Following this introduction of the work, the configuration of the model and the control methodology introduced are described in Section 2. The subsequent section, Section 3, gives full details of the experimental configuration employed for the real-time verification. The presentation and discussion of the results are realized in Section 4, while the final conclusions of this research are shown in Section 5.

2. Configuration and control

This section presents and describes the AC/DC MGC configuration and control, depicted in Fig. 1. The control system is organized in two different levels that separates energy management from electrical execution, ensuring that each technology is operated independently while being coordinated as a whole system. This interaction mechanism, summarized in the flowchart in Fig. 2, consists of two main levels:

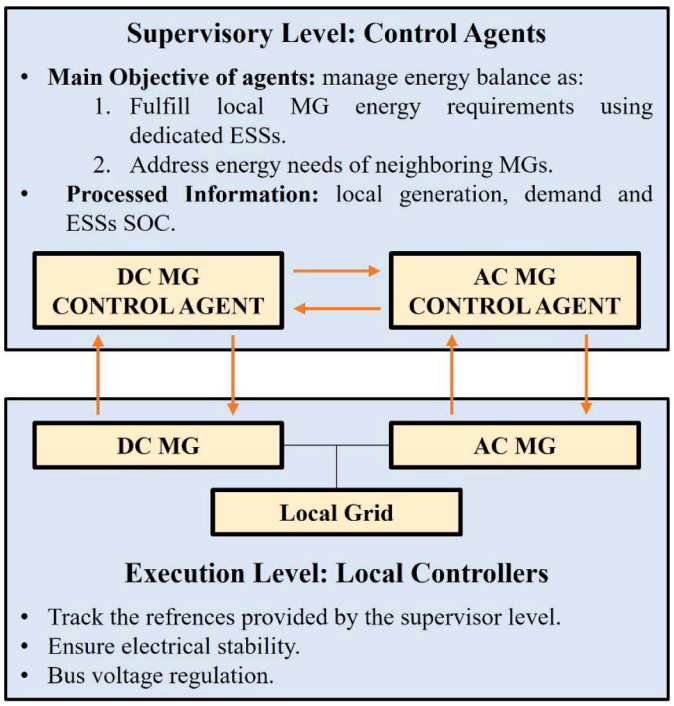

Fig. 2. Control scheme.

- *Supervisory level (control agents):* one agent is assigned to each MG to manage the energy balance at the cluster level. These agents process

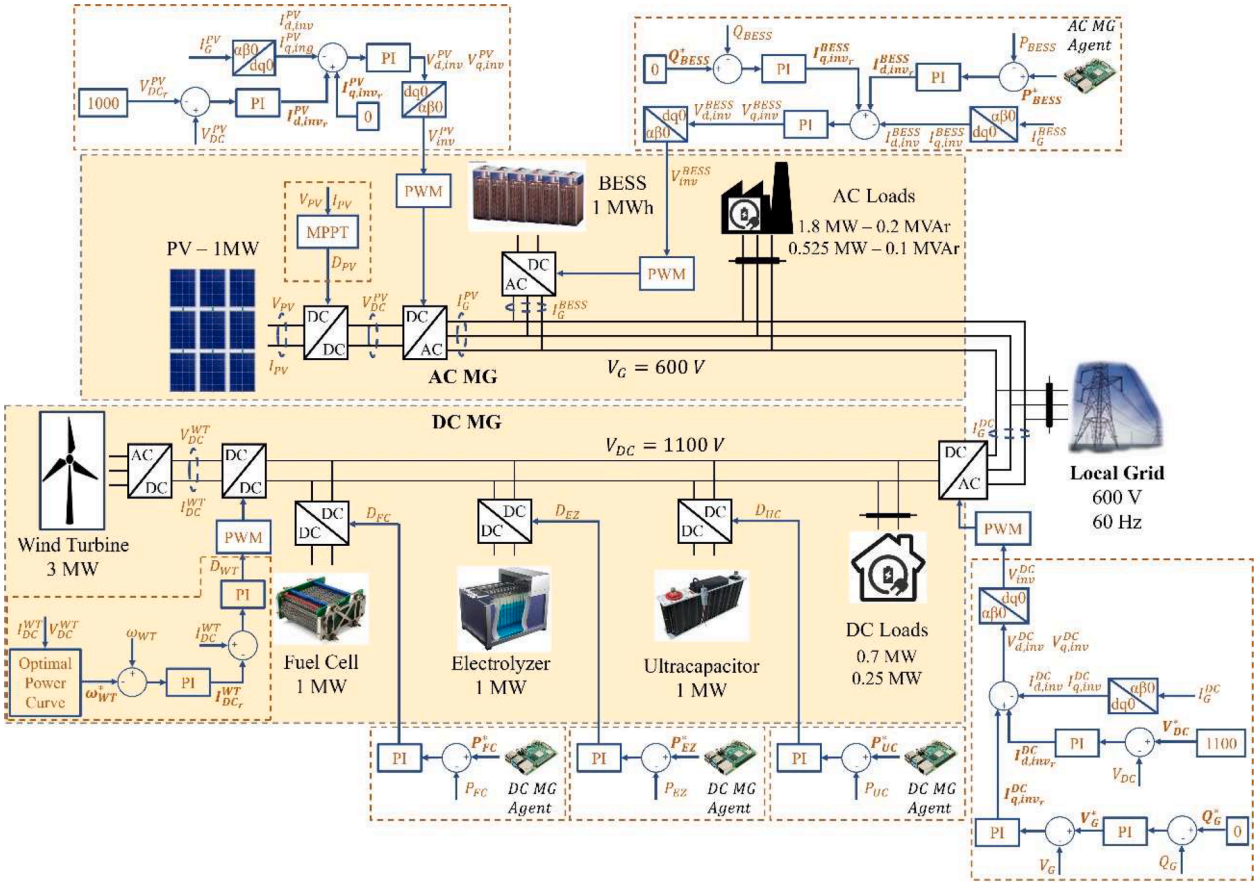

Fig. 1. MGC configuration.

information such as local generation, demand, and the SOC of the ESSs to determine the power distribution strategies.

- *Execution level (local controllers):* these controllers operate at high speed to track the references provided by the supervisory level. They use PI-based control loops to manage the power flow of each converter, ensuring immediate electrical stability and bus voltage regulation.

This division of responsibilities also serves as an intrinsic fallback mechanism to ensure system robustness against communication anomalies, such as data packet dropouts or a complete communication loss. In such events, the local controllers continue to regulate the converters based on the last received valid setpoints. Simultaneously, the local grid, acting as an infinite bus, automatically compensates for any remaining power imbalance within the cluster. This two-fold safety mechanism prevents voltage or frequency instability, ensuring that while distributed optimization might be temporarily unavailable, the fundamental power balance and system integrity are always preserved.

2.1. Local grid

The local grid of the MGC is modelled as a three-phase 600 V voltage supply with a constant voltage at a frequency of 60 Hz, representing an infinite bus. The local grid is connected to the MGC at the node where the two MGs are interconnected. As this voltage source holds the voltage and frequency in that point, no additional control is required. The reactive/active power flow with the AC grid is automatically controlled to ensure energy balance and prevent fluctuations in voltage and frequency.

2.2. DC microgrid

The DC MG is composed of a hydrogen system, with an EZ and a FC, an UC, two DC local loads and a WT interconnected with a common 1100 V DC bus.

A synchronous generator is used to represent the WT of the DC MG with a nominal power of 3 MW [27]. This model is divided into a mechanic sub-model and an electrical sub-model, which is modelled as a sixth-order model. The WT is linked to the DC bus through an uncontrolled rectifier and a DC step-up converter that regulates the WT speed to optimize operation under fluctuating wind speeds.

Regarding the ESSs, the EZ is designed as a DC voltage supply with a series resistance [27], capable of consuming 1 MW. The FC is implemented as a DC voltage supply with a diode [28], and with a rated power of 1 MW [29]. The UC is designed as a series resistance with an ideal capacitor, rated at 1 MW. The UC consists of 5 series elements and 60 parallel branches, with a nominal resistance of 0.018 Ω and a nominal capacitance of 63 F [30].

The ESSs are integrated into the DC MG through controlled converters. A half-bridge converter enables both charging and discharging the UC, enabling bidirectional power flow. As the FC can only supply power to this MG, a step-up converter is applied for this technology. In a similar manner, the EZ uses a buck converter, which can only consume energy.

The constant DC loads are powered by the DC bus without using any converter. One of the loads consumes 0.7 MW, while the other consumes 0.25 MW. An automatic switch is utilized to connect/disconnect each DC load.

This MG is connected to rest of the system through a voltage source inverter (VSI). The VSI of this MG keeps the DC bus voltage (V_{DC}) at 1100 V by compensating the active power fluctuations generated by the wind speed and load fluctuations. It also facilitates the conversion of DC power to AC power for grid integration.

2.3. AC microgrid

The AC MG is constituted by a BESS, a PV power plant and two constant AC loads. A 480/600 V transformer connects this MG to the 600 V AC bus.

The PV power plant is represented as described in [31], using a controlled current source with a parallel diode and resistance and a series resistance, capable of generating 1 MW. It consists of 190 parallel modules and 15 series modules; each rated at 355 Wp. A Perturb and Observe (P&O) method is used to implement the maximum power point tracking (MPPT) technique in a step-up converter, which aims to adjust the DC output voltage of the PV power generator. Furthermore, a VSI inverts this DC power into AC power. Since the PV power generator is integrated into the AC bus, the frequency is set by the grid.

A 1 MW Lithium-Ion BESS is integrated to mitigate fluctuations in PV power generation. The BESS uses cells with a nominal voltage of 3.2 V and a capacity of 14 Ah [32]. It comprises 72 modules connected in series, each containing 4 series-connected cells, resulting in a total voltage of 922 V. Additionally, 80 parallel strings are employed to enhance the system capacity. A VSI connects the BESS to the AC bus, controlling the active and reactive power flow.

The AC MG also includes two constant AC loads. Two three-phase inductive loads are considered, with the first load consuming 525 kW and 100 kVAr, and the second one consuming 1.8 MW and 200 kVAr. To test the dynamics of the MG controllers and control agents across a variety of load conditions, the loads of this MG are connected and disconnected in a non-seasonable form.

2.4. Local controllers

This subsection outlines the local controllers designed for the MGC devices, as illustrated in the schematic diagram in Fig. 1. These controllers are essential for managing the variable power generated and demanded in the system.

For the PV power generator, the P&O algorithm calculates the step-up converter's duty cycle (D_{PV}) using the PV voltage (V_{PV}) and current (I_{PV}) as inputs to maximize energy generation under variable solar irradiance. For the VSI, a cascaded PI-based control loop is implemented in the direct-quadrature (dq) reference frame. In the outer loop, the regulators ensure the PV panels DC voltage tracks its 1000 V reference by adjusting the dq current setpoint of the PV VSI ($I^{PV}_{inv_r}$). Subsequently, the inner loop controls the actual dq current of the PV VSI (I^{PV}_{inv}) by regulating the PV VSI voltage (V^{PV}_{inv}). V^{PV}_{inv} is then modified into the switching signals, using a pulse-width modulation (PWM) generator to introduce it to the VSI.

Regarding the WT, to optimize its power generation despite wind speeds fluctuations, an optimal power curve block utilizes the voltage of the WT (V^{WT}_{DC}) and its current (I^{WT}_{DC}) to generate the speed reference of the WT (ω^{*}_{WT}). This parameter is regulated in a PI controller generating the current reference of the WT ($I^{WT}_{DC_r}$). Then, a second PI controller determines the step-up converter's duty cycle (D_{WT}) to adjust this current, thus ensuring the WT operates along its optimal power curve.

The power flow of each ESS is controlled to track the references produced by each control agent. This action is implemented using PI regulators that adjust each converter's duty cycle (D_{ESS}). For the electric BESS, a cascaded PI-based control loop is implemented. Within this loop, the regulators control the current reactive and active power of the BESS. This involves first adjusting the setpoint of the dq BESS VSI current ($I^{BESS}_{inv_r}$), and then regulating the actual dq current of the BESS VSI (I^{BESS}_{inv}) by modulating the BESS VSI voltage (V^{BESS}_{inv}). Finally, V^{BESS}_{inv} is converted into the switching signals, using a PWM generator to introduce it to the VSI.

Regarding the DC MG VSI, another control loop is also developed. As previously mentioned, V_{DC} is held at 1100 V by setting the dq current

setpoint of the DC MG VSI ($I^{DC}_{inv_r}$). Thus, a PI regulator is used to controll the *dq* current of the DC MG VSI (I^{DC}_{inv}) by setting the voltage of the DC MG VSI (V^{DC}_{inv}). Finally, this voltage is transformed into the switching signals, using a PWM generator to introduce it to the VSI.

The connection/disconnection of the local loads is realized using time-controlled circuit breakers in a non-seasonable form. No specific control strategy is required for these loads, as their demand is considered within the control agents.

2.5. Control agents

Unlike other architectures, distributed control provides key benefits for MGC operation, such as enhanced resilience through the elimination of single points of failure, modular scalability and adaptability, and a significant reduction in communication and computational burden. Moreover, by addressing power imbalances locally, this strategy enables more dynamic and precise control.

As previously mentioned, the two control agents (one per MG) manage the flow of power to ensure balance considering each MG generation and demand as unified reserves. In this sense, the PV power generation and the AC loads contribute to the power generation ($P_{GEN_{AC}}$) and demand ($P_{CON_{AC}}$) of the AC MG, respectively; while the WT energy production and the DC loads contribute to the power generation ($P_{GEN_{DC}}$) and demand ($P_{CON_{DC}}$) of the DC MG, respectively. The primary function of each agent is to fulfill the energy requirements of its respective MG using its dedicated ESSs and second, to address the energy needs of the neighboring MG.

In the AC MG, the state-of-charge (*SOC*) of the BESS is monitored to prevent excessive charge/discharge in the device. In the case of the DC MG, the UC handles fast and transient power imbalances caused by the slow dynamic response of the EZ and FC, and in the case of the hydrogen system, the FC serves as an energy supplier and the EZ as an energy consumer. Lastly, minimum energy production and usage levels are set for the FC and EZ to prevent full disconnection of the devices.

Regarding the DC MG agent, it first checks the power mismatch among $P_{GEN_{DC}}$, $P_{CON_{DC}}$, and the potential power imbalance from the AC MG (ΔP_{AC}), as shown in Eq. (1):

$$\Delta P_{DIF_{DC}} = P_{GEN_{DC}} - P_{CON_{DC}} + \Delta P_{AC} \tag{1}$$

When a positive power imbalance occurs, the EZ is activated to consume excessive energy, and the FC operates at its minimum level. Conversely, if the imbalance is negative, the FC is activated to generate the deficit while the EZ is at its lowest possible level. The active power reference for the UC is subsequently determined by the difference among the combined reference power and the actual output power of the FC and EZ. Assuming perfect regulation of the active power of these technologies, their references and active output powers deviate only temporarily, based on the characteristics of the dynamic response of each technology. Ultimately, if the ESSs of this MG cannot fully compensate for the power mismatch, defined by Eq. (2), the neighboring MG handles this remaining imbalance. The control agent schematic for the DC MG is depicted in Fig. 3a.

$$\Delta P_{DC} = P^{*}_{EZ} + P^{*}_{FC} + P_{GEN_{DC}} - P_{CON_{DC}} \tag{2}$$

For the control agent of the AC MG, the power mismatch among the $P_{CON_{AC}}$ is also checked firstly, as shown in Eq. (3):

$$\Delta P_{DIF_{AC}} = P_{GEN_{AC}} - P_{CON_{AC}} + \Delta P_{DC} \tag{3}$$

When a positive power imbalance occurs, the BESS is utilized to absorb excess energy. Conversely, if the imbalance is negative, the BESS discharges to supply energy. In a second step, the BESS SOC is monitored to calculate its capacity to supply or store energy. When a high SOC is produced, the BESS cannot absorb energy. Similarly, if the SOC is low, it cannot discharge further. When a medium SOC is produced, the BESS can supply or store energy based on its actual SOC. Finally, if the BESS is unable to fully offset the power imbalance given by Eq. (4), the other MG tries to address this imbalance. Fig. 3b shows the strategy implemented for the AC MG control agent.

$$\Delta P_{AC} = P_{GEN_{AC}} - P_{CON_{AC}} + P^{*}_{BESS} \tag{4}$$

Finally, the local grid ensures the energy balance within the MGC when the collective capacity of the ESSs in each MG is unable to manage the internal power imbalances.

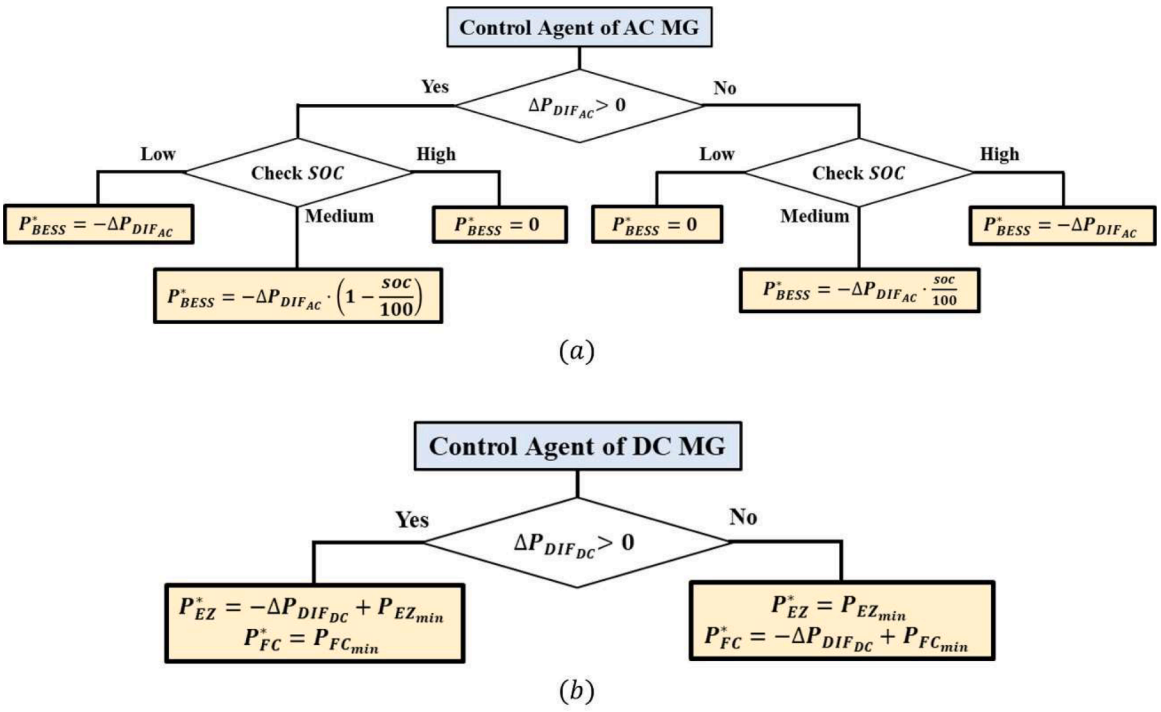

Fig. 3. Control agents: (a) AC MG; and (b) DC MG.

2.5.1. Control agents scalability and adaptability

Although this study focuses on a specific MGC comprising two MGs, this subsection examines the inherent scalability of the proposed distributed control architecture and its capacity to integrate supplementary MGs.

When a new MG is integrated into the MGC, a dedicated control agent is deployed with the same dual objectives: first, to fulfill the energy requirements of its respective MG using its dedicated ESSs; and second, to support the energy needs of neighboring MGs. To facilitate this control strategy, the different generation and consumption technologies within a given MG are aggregated into a single generation pool and a single consumption pool for that MG, respectively.

Thus, the control agent of the MG i first checks the power mismatch among the generated power (P_{GEN_i}) and consumed power (P_{CON_i}) of that MG and the sum of the proportional power mismatches from its adjacent MGs. For each adjacent MG j, this proportion is defined as its possible power mismatch (ΔP_j) divided by its respective number of neighboring MGs (n_j), as shown in Eq. (5):

$$\Delta P_{DIF_i} = P_{GEN_i} - P_{CON_i} + \sum_{j=1}^{j=k} \frac{\Delta P_j}{n_j} \tag{5}$$

In the second step, ΔP_{DIF_i} is distributed among the ESSs within the MG i in a similar manner to the original control agents. Ultimately, if the ESSs of the MG i cannot fully compensate for the power mismatch, defined by Eq. (6), the neighboring MGs handle this remaining imbalance.

$$\Delta P_i = P_{GEN_i} - P_{CON_i} + P^*_{ESS_i} \tag{6}$$

Finally, as the original control agents, the local grid ensures the energy balance within the MGC when the collective capacity of the ESSs in each MG is unable to manage the internal power imbalances.

3. Experimental configuration

3.1. Experimental setup

As depicted in Fig. 4, the experimental setup employs two RPi boards and an OPAL-RT unit integrated into a communication network, along with a host PC and an oscilloscope.

The OPAL-RT 4512 unit is a HIL emulation system that enables real-time simulation of the MGC by interfacing Simulink models with real-time hardware. For this purpose, OPAL-RT provides the RT-LAB software platform, which allows users to create, execute and monitor models within a single and integrated simulation environment.

The RPi 4B board is an affordable single-board computer that can be used and programmed in Python language. In this work, it provides a platform for developing and deploying for MG control and management. Python 3.7 is the programming language selected herein. Two RPi boards are utilized for executing each MG control agent.

In this research, the MGC and the local controllers are designed in MATLAB 2022a and deployed on the OPAL-RT unit via RT-LAB 2023.1. A host PC monitors the entire simulation and manages the communication process. To enhance the computational efficiency and ensure real-time emulation, the MGC model is structured into three subsystems: Slave, Master, and Scope.

Finally, a Yokogawa DLM 4038 oscilloscope completes the experimental setup. This device allows measuring and displaying the experimental results. For an accurate visualization of the signals on the oscilloscope, the measurements are scaled down to fit in the analogue output range of the OPAL-RT 4512 unit. This range, operating between −16 V and 16 V, ensures proper representation of the measurements on the oscilloscope.

This experimental setup provides a rapid prototyping platform and represents effectively the complex relationships within the system.

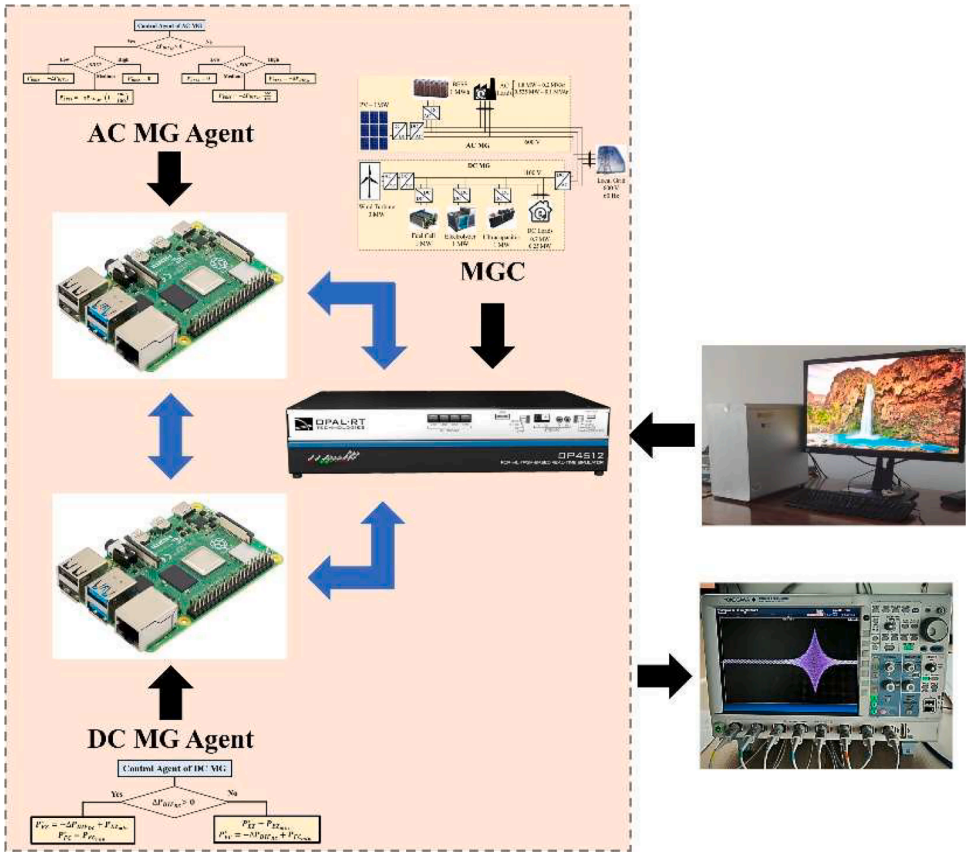

Fig. 4. Experimental setup.

3.2. Data communication protocol

For execution, a reliable communication protocol is crucial for facilitating information transfer between the devices in the experimental setup.

For such purposes, OPAL-RT offers recognized communication protocols. Notably, Modbus is a prevalent standard for real-time communication in industrial and energy systems owing to its increased reliability and error handling capabilities, among other features [33]. This protocol is based on a master-slave communication structure.

Using this communication protocol, the RPi boards and the OPAL-RT simulator communicate over an ethernet network. Each device is assigned a unique IP address, and communication links are established via dedicated Modbus ports. Since each of the three devices can be configured to have two Modbus ports, it can establish a direct link with the other two, ensuring seamless data flow. Thus, to enable the communication, the correct IP addresses and Modbus port numbers must be programmed into each equipment. Regarding the master-slave structure, the OPAL-RT simulator is the master device and the RPi boards are the slave devices.

The information transfer process is as follows: each RPi board receives the generated and demanded energy measurements, the status of the local ESSs, and any potential power mismatch from the neighboring MG. Within each RPi board, the agent calculates the power references for each ESS and the potential power mismatch of its respective MG. Ultimately, the calculated references are returned by RPi boards.

The data exchange rate is restricted by the OPAL-RT emulator decimation factor (500) and the simulation time step (50 μs), resulting in an effective update period of 25 ms (50 μs x 500). To confirm that the computation and communication cycle is consistent with this rate, the round-trip time was measured experimentally over 350 samples on each RPi board. This parameter represents the time required for an RPi board to execute a complete control cycle. The recorded average round-trip is 0.959 ms, with a standard deviation of 0.296 ms, for the AC MG RPi board; while the average for the DC MG RPi is 0.759 ms, with a standard deviation of 0.364 ms. These results confirm that the control cycle is consistent with the data exchange rate. Furthermore, the risk of control failure due to time-scale mismatches is mitigated by multi-level control architecture: while the control agents manage the power balance every 25 ms, the local controllers ensure the electrical stability every 50 μs.

4. Results and discussion

The experimental configuration is utilized in this section to emulate the MGC and validate the performance of the system and its control methodology. For this reason, three distinct scenarios are considered across different working scenarios in the real-time and simulation tests. In the first scenario (Section 4.1), the MGC and its control are experimentally evaluated over a 10-second test without any communication latency. The second scenario (Section 4.2) presents a comparative study between the proposed distributed strategy and a centralized control approach, conducted under the same simulation conditions as the first case. Finally, the third scenario (Section 4.3) introduces several communication latencies to assess their impact on the system behavior over a 20-second test. Identical changes in the working conditions are spaced proportionally to the duration of each test; that is, an event occurring at time t in the 10-second test appears at time $2{\cdot}t$ in the 20-second test.

The tests simulate different dynamic conditions by varying renewable generation (PV and WT) via solar irradiance and wind speed profiles. The demand is also adjusted via loads switching at specific intervals. In all test cases, the BESS starts at a SOC of 50%.

To ensure an accurate representation on the oscilloscope, most signals, excluding V_{DC}, are scaled down by a factor of $1{\cdot}10^6$. V_{DC} is scaled down by a factor of 600.

4.1. No-latency test

This section presents the experimental results obtained under zero communication latency. Fig. 5a depicts P_{WT},$P_{Load_{DC}}$ and ΔP_{AC}. As evidenced, P_{WT} varies throughout the experimental test due to fluctuations in the wind speed. Similarly, $P_{Load_{DC}}$ varies with the management of local loads connections to the DC bus. Although the local loads are fixed as constant power loads, slight fluctuations in $P_{Load_{DC}}$ occur due to minor voltage variations on the DC bus. This problem is mitigated on the AC bus by the presence of the local grid.

The evolution of ΔP_{AC} shows that there is a power mismatch within the MG throughout the test. This mismatch may arise from the BESS's inability to maintain power balance within the AC MG or the restriction of available power imposed by its SOC.

Fig. 5b presents the power flow among the DC MG ESSs and their reference values. Firstly, it can be observed that the local controllers perform well, as all devices represented in this figure accurately track their active power setpoints. In addition, they comply with their functions correctly, as the FC compensates for the power deficit between 2.5 s to 3 s, while the EZ remains at its minimum inactive level. Conversely, the EZ absorbs surplus energy during intervals of power surplus generation, with the FC remaining at its minimum inactive level. A key observation is that the EZ operates at full capacity from 0 to 2.5 s, making it unable to consume any additional energy, producing a power imbalance in this MG. Finally, the UC effectively manages transient conditions with significant power excursions, which gradually return to zero as the DC MG stabilizes.

V_{DC} is represented in Fig. 6. The results of the test confirm the correct voltage regulation around the setpoint value. As expected, sudden active power variations in the DC MG result in variations on the bus voltage, which are satisfactorily regulated by the local controllers of the DC MG VSI.

$P_{Load_{AC}}$,P_{PV} and ΔP_{DC} are illustrated in Fig. 7a. As observed, P_{PV} varies with solar irradiance while$P_{Load_{AC}}$ varies based on load disconnection/connection from the AC bus.

The evolution of ΔP_{DC} indicates a power imbalance during the initial phase of the test, which is corrected by t = 2.5 s. This mismatch occurs because the EZ cannot absorb enough active power to balance the DC MG, as depicted in Fig. 5b

The setpoint for active power flow of the BESS and its actual value are shown in Fig. 7b Firstly, the results clearly show that the local controllers perform well, as the BESS accurately tracks its active power setpoints. Furthermore, when there is a surplus of energy demanded in the AC MG, the BESS supplies energy (around between 1.5 and 3.75 s, and 5 and 10 s) and stores energy during the rest of the test. Given its initial 50% SOC, this device is capable of supplying and absorbing energy based on its actual SOC, thereby addressing the power imbalance within this MG.

Fig. 8 illustrates the active power flow exchanged with the local grid. The grid intervenes whenever the ESSs of the system are unable to restore the energy balance due to power fluctuations across the different scenarios. As depicted in the figure, the grid absorbs and supplies the different mismatches during transient periods. Once the power balance is restored in both MGs, the power flow with the grid tends to zero.

4.2. Comparative study: distributed vs. centralized control

This subsection presents a comparative study between the proposed distributed control architecture (denoted as distributed EMS, D-EMS) and an alternative centralized control agent architecture (denoted as centralized EMS, C-EMS), as illustrated in Fig. 9. The C-EMS focuses on managing the global power mismatch between the total generation and demand by coordinating the available ESSs to ensure their efficient utilization. Consequently, all generation technologies contribute to a unified generation pool, while consumption technologies are integrated

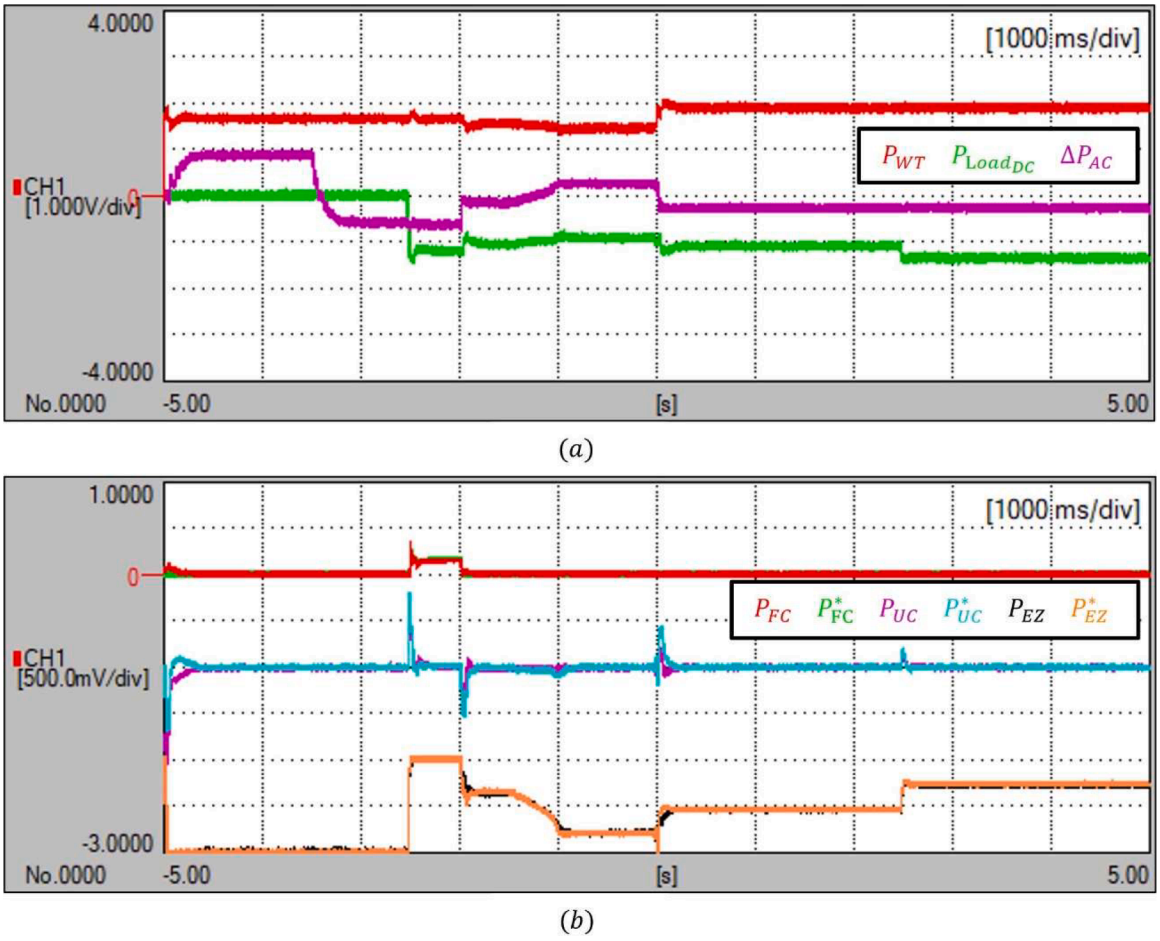

Fig. 5. Active power flow in the DC MG: (a) Generation, demand and AC MG power mismatch; and (b) ESSs.

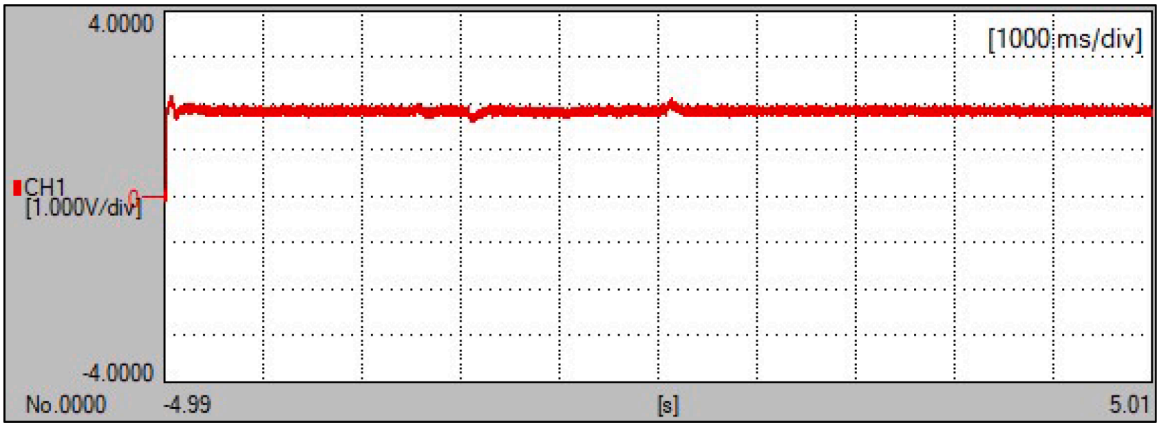

Fig. 6. DC bus voltage.

into a unified consumption pool.

Following these premises, the total generation and demand of the MGC are compared. If the demand exceeds generation, the ESSs compensate for the energy deficit; conversely, when generation surpasses demand, the surplus energy is stored within the ESSs. In a second step, the BESS SOC is monitored to calculate its available capacity. If a high SOC is detected, the excess energy is absorbed by the EZ, as the BESS cannot store additional energy. Similarly, if the SOC is low, the BESS cannot discharge further, and the FC provides the necessary power to meet the power mismatch. When a SOC is within a medium range, the BESS and the hydrogen system collaboratively address the power mismatch within the MGC. Finally, P^*_{UC} is computed by calculating the deviation between the actual output of the remaining ESSs and their respective reference values. As previously established, the objective of the UC is to rapidly mitigate the transient power mismatches.

Fig. 10 presents P_{GEN}, P_{CON} and P_{PCC} for both EMSs. As previously established, both EMSs are evaluated under the same simulation conditions to ensure that the generation and demand profiles remain identical across both simulations. However, the variations observed in the signals of the DC MG are primarily attributed to fluctuations in V_DC,

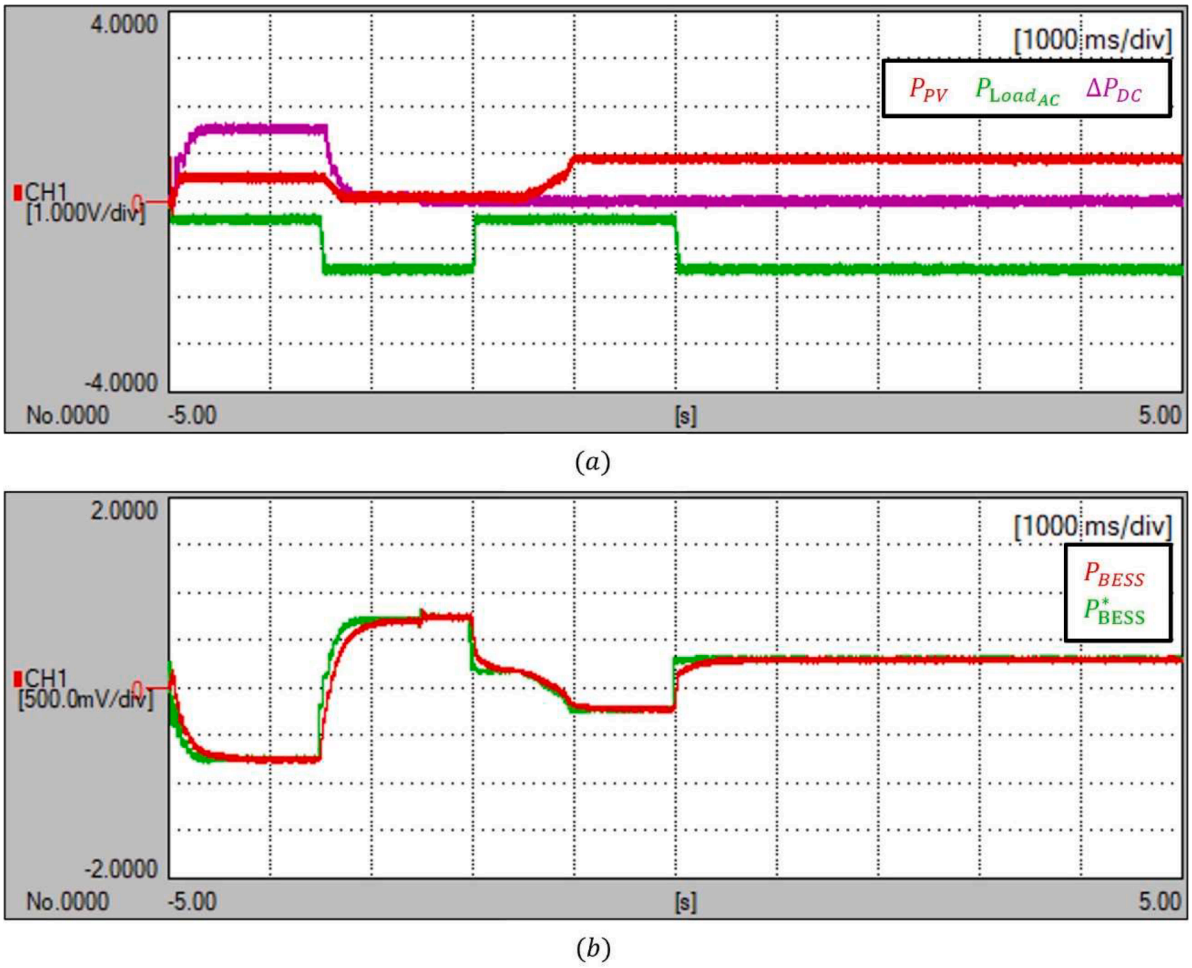

Fig. 7. Active power flow in the AC MG: (a) Generation, demand and DC MG power mismatch; and (b) ESSs.

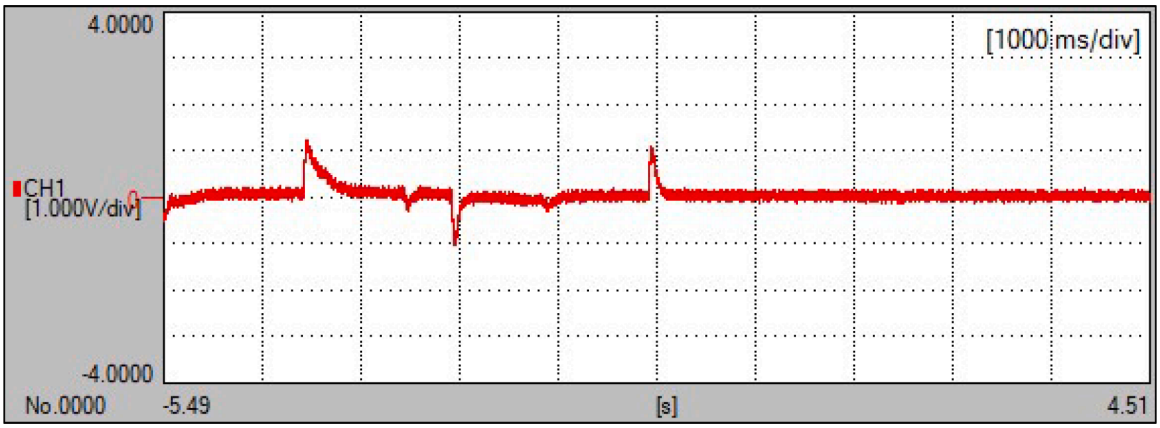

Fig. 8. Flow of active power with the local grid.

as illustrated in Fig. 12.

Similarly, the local grid compensates for power mismatches of the MGC and handles transitory states for the EMSs. In both cases, the active power flow between the MGC and the local grid remains close to zero compared to the internal MGC generation and demand. However, the proposed D-EMS achieves a slight reduction of 1.30% in the total net energy exchanged with the local grid (E_{Grid}), as shown in Table 2. These differences arise from the distinct utilization of the ESSs based on the nature of the control architecture.

Fig. 11 presents the power flow of the ESSs and their corresponding reference values for both EMSs. It can be observed that the local controllers perform effectively in both controls, as all devices accurately track their active power setpoints. The observed differences arise solely from the distinct architecture employed in each control agent.

A significant difference between the EMSs lies in the role of the ESSs, whose energy usage is detailed in Table 2. In this regard, the behavior of the ESSs under the D-EMS follows the logic described in Section 4.1: they are managed to independently address the local power mismatch of their

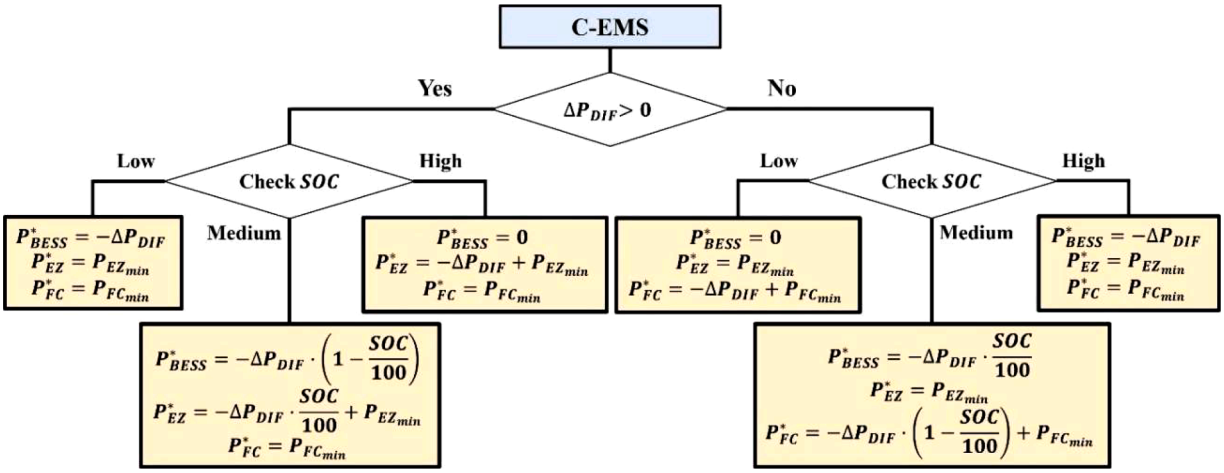

Fig. 9. Centralized energy management system.

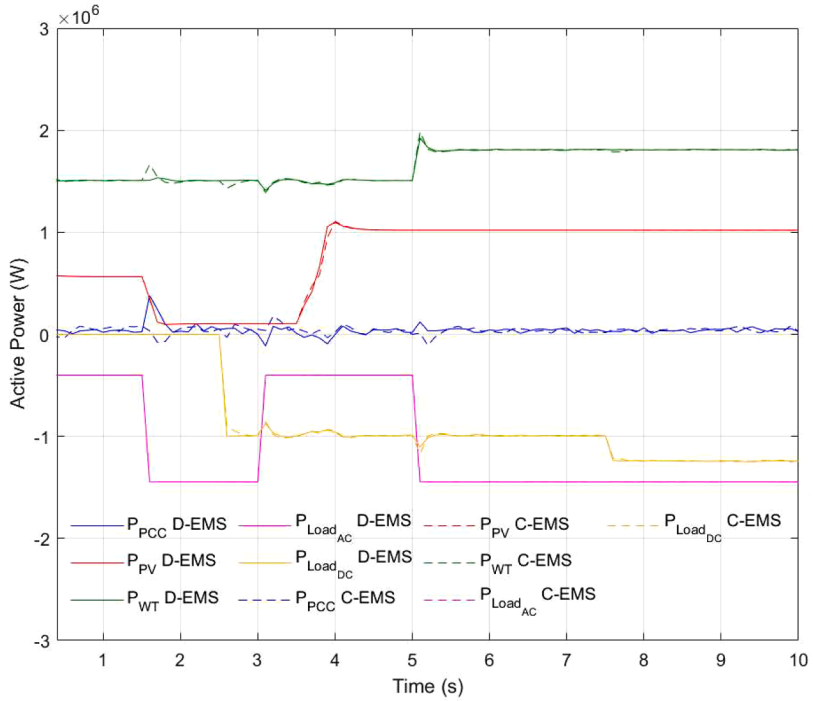

Fig. 10. Generation, demand and flow of active power with the local grid for both EMSs.

Table 2
Comparison of parameters for both EMSs.

Parameters	Distributed architecture (D-EMS)	Centralized architecture (C-EMS)	Δ (%) D-EMS vs. C-EMS
E_{Grid} (**kWh**)	0.116	0.118	−1.30
E_{BESS} (**kWh**)	0.192	−0.731	−73.68
E_{EZ} (**kWh**)	−1.712	−0.818	109.20
E_{FC} (**kWh**)	0.0270	0.0632	−57.19
E_{UC} (**kWh**)	−0.0109	−0.0155	−29.56
$ITAE_{BESS}$ (**kWh**)	0.170	0.180	−5.28
$ITAE_{EZ}$ (**kWh**)	0.0568	0.0755	−24.81
$ITAE_{FC}$ (**kWh**)	0.0124	0.167	−25.74
$ITAE_{UC}$ (**kWh**)	0.110	0.161	−31.93
$ITAE_{V_{dc}}$ (**Vs**)	217.5	324	−32.87
$ITAE_{Grid}$ (**kWh**)	0.641	0.665	−3.64

respective MG, and secondarily support the neighboring MG. Consequently, as shown in Table 2, the BESS is utilized less under the D-EMS, since its primary role is to cover the specific power mismatch in the AC MG.

Meanwhile, under the C-EMS, the BESS and the hydrogen system collaboratively address the power mismatch within the MGC, owing to the medium SOC level maintained during the test. This fact provides the C-EMS enough operational margin to share the power mismatch. Consequently, the BESS in the C-EMS is forced to handle much larger power fluctuations, as it not only addresses the AC MG power mismatches but also cooperates to manage the DC MG power mismatches.

The architectural difference also impacts the hydrogen system behavior. Because the DC MG generation exceeds its demand, the EZ in the D-EMS exhibits higher power consumption to locally manage this surplus. In contrast, this surplus is partially absorbed by the BESS in the C-EMS, leading to a lower consumption by the EZ. Similarly, the FC generates less energy in the D-EMS compared to the C-EMS. In the D-EMS, the FC only acts as a backup to cover the AC MG power mismatch,

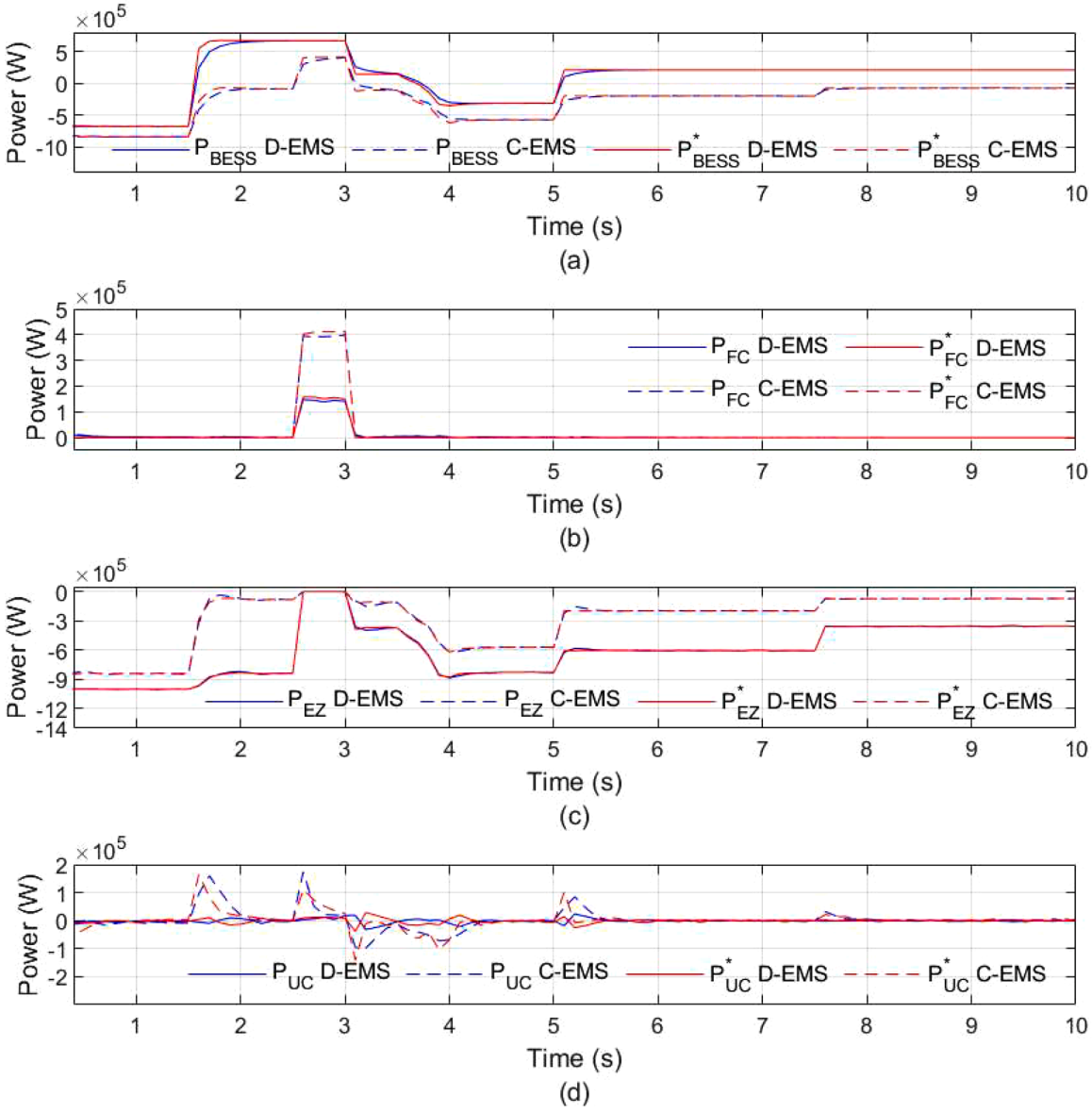

Fig. 11. Active power flow in the ESSs for both EMSs: (a) BESS, (b) FC, (c) EZ and (d) UC.

whereas the C-EMS uses it more to balance the overall MGC power mismatch.

Finally, the UC effectively manages transient conditions involving significant power excursions, which gradually return to zero as the DC MG ESSs stabilize under the D-EMS, and as all the MGC ESSs stabilize under the C-EMS.

V_{DC} is represented in Fig. 12. The test results confirm the correct voltage regulation around the setpoint under both control architectures. As previously noted, sudden active power variations within the DC MG result in fluctuations in the bus voltage.

Table 2 presents a comparison of the total net energy exchanged with the local grid and the various ESSs (E), as well as the ITAE of the ESSs powers, V_{DC}, and the active power exchanged with the local grid. The results indicate an improvement in the ITAE metrics under the D-EMS compared to the C-EMS. Specifically, reductions of 5.28% in $ITAE_{BESS}$, 25.74% in $ITAE_{FC}$, 31.93% in $ITAE_{UC}$, 24.81% in $ITAE_{EZ}$, 32.87% in $ITAE_{V_{DC}}$ and 3.264% in $ITAE_{Grid}$ are achieved. These improvements are primarily attributed to the distributed nature of the control, which enables the local processing of power mismatches within each MG, providing more precise tracking of the setpoint signals compared to the C-EMS.

4.3. Latency tests

As previously mentioned, this subsection presents the impact of communication latencies on the control agents. Three tests are conducted using identical latency for all the inputs and outputs of the control agents. The latencies are defined based on the standards in [34], reproducing a low latency test (15 ms), a mid latency test (60 ms) and a high latency test (200 ms).

Figs. 13,14 represent the system behavior under the three aforementioned latency scenarios. Since the generated and consumed power values are unaffected by the communication latency, they are not illustrated. As latency duration increases, deviations from non-latency scenario also increase due to the delayed execution of the control strategies. The controllers receive and transmit signals with a certain delay, which affects all the signals represented. Despite these latencies, the system remains stable, as the local grid helps maintain power balance. However, a notable consequence is the increased dependence of the MGC on the grid as the latency rises, as shown in Table 3.

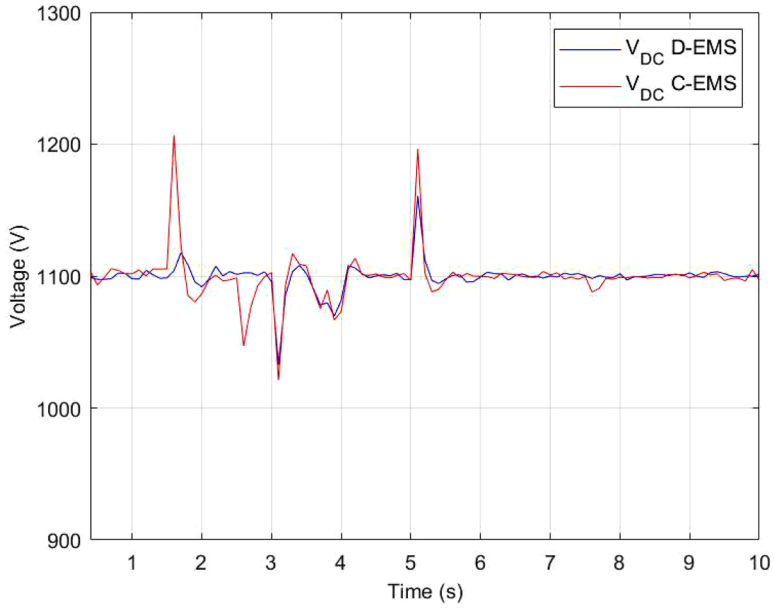

Fig. 12. DC bus voltage for both EMSs.

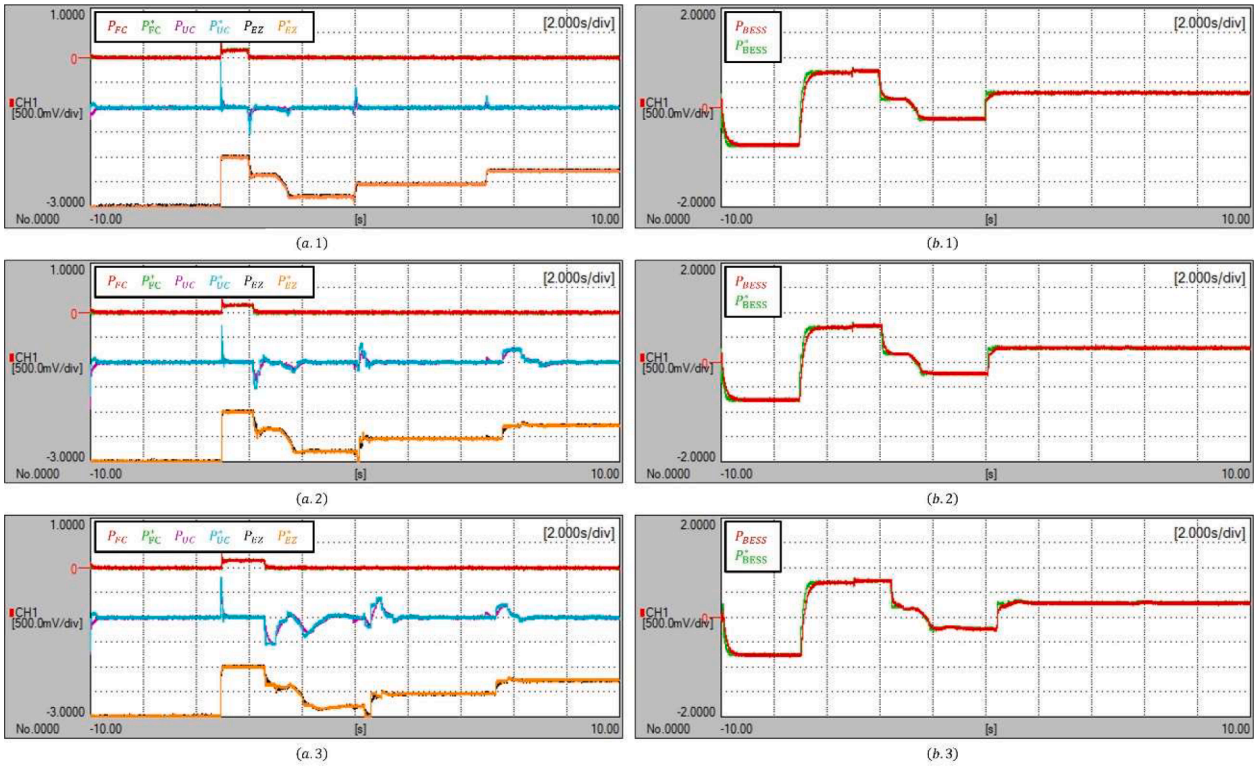

Fig. 13. Active power flow in the ESSs considering latencies in inputs and outputs of the control agents: (a.1)-(b.1) 15 ms, (a.2)-(b.2) 60 ms, and (a.3)-(b.3) 200 ms.

Table 3 presents a comparison of the total net energy exchanged with the local grid and the various ESSs (E), as well as the ITAE of the ESS powers, V_{DC} and the active power exchanged with the local grid. The results indicate that the ITAE worsen with higher latency due to the delayed controller action and the resulting increase in overshoot and settling time of the system. In terms of energy, the delayed actuation leads to an increased use of the ESSs, resulting in greater net energy flows among them. Consequently, net energy flow with the local grid decreases as latency increases. Therefore, although the power flow with the local grid diminishes with rising latencies, the increased net energy flow among the ESSs leads to higher ITAE values, indicating greater dependence of the MGC on the local grid.

5. Conclusion

This work demonstrated that a novel distributed control strategy effectively managed a real-time MGC. The MGC consisted of a DC MG (comprising FC, UC, WT, EZ and DC loads) and an AC MG (including BESS, AC loads, and PV power plant). The control architecture integrated an execution layer (local controllers), which was essential for

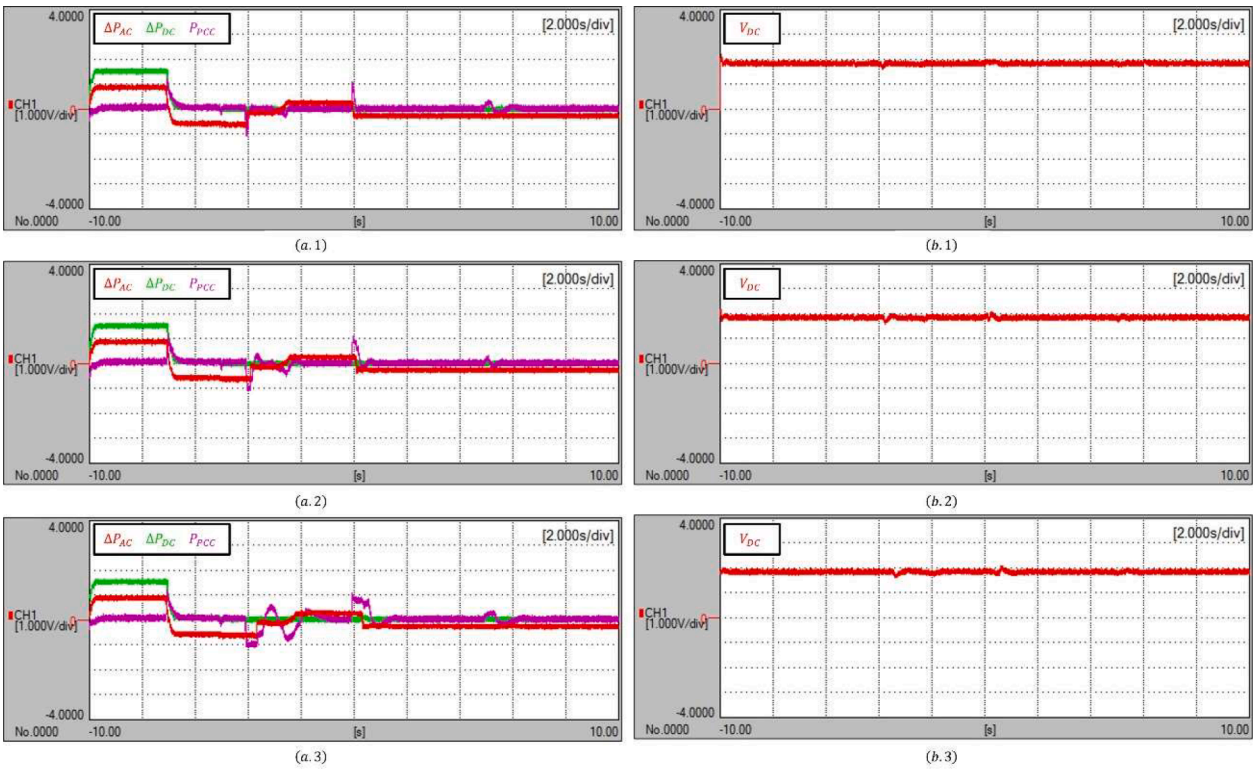

Fig. 14. MGC performance considering latencies in inputs and outputs of the control agents: (a.1)-(b.1) 15 ms, (a.2)-(b.2) 60 ms, and (a.3)-(b.3) 200 ms.

Table 3
Comparison of parameters for the different latencies.

Time Latency	0 ms	15 ms (Low)	Δ (%)	60 ms (Mid)	Δ (%)	200 ms (High)	Δ (%)
E_{Grid} (**kWh**)	0.234	0.230	−1.90	0.217	−7.39	0.1824	−22.10
E_{BESS} (**kWh**)	0.645	0.649	0.63	0.661	2.59	0.706	9.56
E_{EZ} (**kWh**)	−3.261	−3.258	−0.09	−3.250	−0.34	−3.228	−1.02
E_{FC} (**kWh**)	0.0500	0.0520	3.94	0.0579	15.77	0.0764	52.69
E_{UC} (**kWh**)	−0.0145	−0.0181	24.56	−0.0289	98.78	−0.0624	329.66
$ITAE_{BESS}$ (**MWs**)	1.23	1.26	2.44	1.29	4.55	1.41	14.22
$ITAE_{EZ}$ (**MWs**)	0.151	0.153	1.33	0.159	5.23	0.174	15.50
$ITAE_{FC}$ (**MWs**)	0.624	0.609	−2.44	1.00	60.65	1.38	121.74
$ITAE_{UC}$ (**MWs**)	1.21	1.20	−1.32	2.00	64.28	2.77	128.74
$ITAE_{V_{dc}}$ (**Vs**)	652	646	−0.92	938.9	44.00	1260	93.25
$ITAE_{Grid}$ (**MWs**)	7.70	8.12	−5.41	11.4	48.12	22.8	196.25

tracking setpoints and maintaining electrical stability within the individual MGC devices, and a supervisory layer (distributed control agents), which exhibited robust performance and successful operation. These agents were executed on two RPi boards (one per MG) and interfaced via Modbus with an OPAL-RT unit, which emulated the MGC and its local controllers.

A contribution of this work was demonstrating the enhanced performance of the distributed approach over a centralized architecture. By processing power mismatches locally within each MG, the system achieved more precise setpoint tracking, as evidenced by the significant reductions in ITAE metrics. Furthermore, this architecture offered unique advantages, such as enhanced resilience by eliminating single points of failure, and ensured modular scalability, allowing for the integration of new MGs without increasing the centralized computational burden.

Additionally, the impact of communication latencies on control agent performance was assessed under three standard-aligned test cases: 15 ms, 60 ms and 200 ms. While higher latencies led to increased peak power usage from the local grid due to delayed responses, the total net energy exchange decreased, driven by more intensive ESSs usage. Despite the performance degradation induced by these latencies, system stability was maintained across all test cases. Furthermore, the implementation of the local grid as an infinite bus served as a robust intrinsic fallback mechanism to provide system integrity even during potential communication failures.

While the experimental validation based on HIL confirmed the effectiveness of the proposed control strategy, certain limitations remained. Therefore, future works could focus on evaluating the distributed control strategy within larger MGCs, integrating economic criteria into the control agents to minimize operational costs, or investigating the control behavior during the transition to islanded mode.

CRediT authorship contribution statement

David Carrasco-González: Writing – original draft, Visualization, Validation, Software, Resources, Methodology, Investigation, Formal analysis, Data curation, Conceptualization. **Raúl Sarrias-Mena:** Writing – original draft, Visualization, Validation, Software, Resources, Methodology, Investigation, Conceptualization. **Pablo Horrillo-Quintero:** Writing – original draft, Visualization, Validation, Software, Resources,

Methodology, Investigation, Formal analysis, Conceptualization. **Ehsan Hosseini:** Writing – original draft, Validation, Software, Resources, Methodology, Investigation, Formal analysis, Conceptualization. **Francisco Llorens-Iborra:** Writing – original draft, Visualization, Validation, Software, Resources, Methodology, Investigation, Formal analysis, Conceptualization. **Luis M. Fernández-Ramírez:** Writing – review & editing, Writing – original draft, Visualization, Validation, Supervision, Project administration, Methodology, Investigation, Funding acquisition, Formal analysis, Conceptualization.

Declaration of competing interest

The authors declare that they have no known competing financial interests or personal relationships that could have appeared to influence the work reported in this paper.

Acknowledgments

This work was partially supported by Ministerio de Ciencia e Innovación, Agencia Estatal de Investigación, FEDER, UE (Grant PID2021-123633OB-C32 supported by MCIN /AEI /10.13039/501100011033/FEDER, UE).

Data availability

Data will be made available on request.

References

[1] J. Zhou, Z. Weng, J. Li, X. Song, Reliability evaluation, planning, and economic analysis of microgrid with access to renewable energy and electric vehicles, Electr. Power Syst. Res. 230 (2024) 110252, https://doi.org/10.1016/J.EPSR.2024.110252.

[2] S. Patel, A. Ghosh, P.K. Ray, Adaptive power management in PV/Battery integrated hybrid microgrid system, in: PESGRE 2022 - IEEE International Conference on "Power Electronics, Smart Grid, and Renewable Energy, 2022, https://doi.org/10.1109/PESGRE52268.2022.9715905.

[3] Y. Shen, J. Zhai, Z. Kang, B. Zhao, X. Gao, Z. Li, Distributionally robust chance-constrained energy management for island DC microgrid with offshore wind power hydrogen production, Energy 316 (2025) 134570, https://doi.org/10.1016/J.ENERGY.2025.134570.

[4] C.E. da Matta, E.V. do, N. De Lorenci, J.A. da Silva Neto, A.C. Zambroni de Souza, P.P. Balestrassi, Designing a near-optimal isolated microgrid using active learning, Electr. Power Syst. Res. 250 (2026) 112055, https://doi.org/10.1016/J.EPSR.2025.112055.

[5] Y. Lv, X. Dou, C. Zhang, Q. Bu, P. Lv, A feasible grid-switching model predictive control approach for frequency and voltage safety of microgrid clusters, Electr. Power Syst. Res. 248 (2025) 111865, https://doi.org/10.1016/J.EPSR.2025.111865.

[6] F.N. Budiman, M.A.M. Ramli, H.R.E.H. Bouchekara, A.H. Milyani, Optimal scheduling of a microgrid with power quality constraints based on demand side management under grid-connected and islanding operations, Int. J. Electr. Power Energy Syst. 155 (2024) 109650, https://doi.org/10.1016/J.IJEPES.2023.109650.

[7] F. Fachini, T. Bogodorova, L. Vanfretti, S. Boersma, A microgrid control scheme for islanded operation and re-synchronization utilizing model predictive control, Sustain. Energy Grids Netw. 39 (2024) 101464, https://doi.org/10.1016/J.SEGAN.2024.101464.

[8] S. Tsianikas, J. Zhou, N. Yousefi, M.D. Rodgers, D.W. Coit, Multi-energy microgrid expansion planning with reliability consideration based on deep reinforcement learning, Comput. Ind. Eng. 207 (2025) 111283, https://doi.org/10.1016/J.CIE.2025.111283.

[9] B. Chen, J. Wang, X. Lu, C. Chen, S. Zhao, Networked Microgrids for Grid Resilience, Robustness, and Efficiency: A Review, Institute of Electrical and Electronics Engineers Inc, 2021, https://doi.org/10.1109/TSG.2020.3010570.

[10] F. Bandeiras, E. Pinheiro, M. Gomes, P. Coelho, J. Fernandes, Review of the Cooperation and Operation of Microgrid Clusters, Elsevier Ltd, 2020, https://doi.org/10.1016/j.rser.2020.110311.

[11] H. Rasoulinezhad, M. Abapour, O. Sadeghian, K. Zare, The role of risk-based demand response in resource management of a grid-connected renewable-based large-scale microgrid with stationary and mobile energy storage systems and emission tax, Comput. Ind. Eng. 183 (2023) 109555, https://doi.org/10.1016/J.CIE.2023.109555.

[12] Y. Ennassiri, G. Ferro, D. Bellotti, L. Magistri, M. Robba, Optimal scheduling and real-time control of a microgrid with an electrolyzer and a fuel cell systems using a reference governor approach, Sustain. Energy Grids Netw. 36 (2023) 101218, https://doi.org/10.1016/J.SEGAN.2023.101218.

[13] T. Sattarpour, S. Golshannavaz, D. Nazarpour, P. Siano, A multi-stage linearized interactive operation model of smart distribution grid with residential microgrids, Int. J. Electr. Power Energy Syst. 108 (2019) 456–471, https://doi.org/10.1016/J.IJEPES.2019.01.023.

[14] E. Espina, J. Llanos, C. Burgos-Mellado, R. Cárdenas-Dobson, M. Martínez-Gómez, D. Sáez, Distributed control strategies for microgrids: an overview, IEEE Access 8 (2020) 193412–193448, https://doi.org/10.1109/ACCESS.2020.3032378.

[15] J. Lu, B. Zhang, X. Hou, J.M. Guerrero, A distributed control strategy for unbalanced voltage compensation in islanded ac microgrids without continuous communication, IEEE Trans. Ind. Electron. 70 (3) (2023) 2628–2638, https://doi.org/10.1109/TIE.2022.3169841.

[16] J.W. Simpson-Porco, Q. Shafiee, F. Dorfler, J.C. Vasquez, J.M. Guerrero, F. Bullo, Secondary frequency and voltage control of islanded microgrids via distributed averaging, IEEE Trans. Ind. Electron. 62 (11) (2015) 7025–7038, https://doi.org/10.1109/TIE.2015.2436879.

[17] W. Kang, J. Liao, M. Chen, K. Sun, P.J. Tavner, J.M. Guerrero, Distributed optimal power management for smart homes in microgrids with network and communication constraints, Appl. Energy 375 (2024) 124102, https://doi.org/10.1016/J.APENERGY.2024.124102.

[18] L. Huang, W. Sun, Q. Li, W. Li, Distributed real-time economic dispatch for islanded microgrids with dynamic power demand, Appl. Energy 342 (2023) 121156, https://doi.org/10.1016/J.APENERGY.2023.121156.

[19] L. Li, M. Dong, D. Song, J. Yang, Q. Wang, Distributed and real-time economic dispatch strategy for an islanded microgrid with fair participation of thermostatically controlled loads, Energy 261 (2022) 125294, https://doi.org/10.1016/J.ENERGY.2022.125294.

[20] S. Moayedi, A. Davoudi, Distributed tertiary control of DC microgrid clusters, IEEE Trans. Power Elect. 31 (2) (2016) 1717–1733, https://doi.org/10.1109/TPEL.2015.2424672.

[21] M. Zaery, P. Wang, W. Wang, D. Xu, Distributed global economical load sharing for a cluster of DC Microgrids, IEEE Trans. Power Syst. 35 (5) (2020) 3410–3420, https://doi.org/10.1109/TPWRS.2020.2975378.

[22] X. Lu, J. Lai, X. Yu, Y. Wang, J.M. Guerrero, Distributed coordination of islanded microgrid clusters using a two-layer intermittent communication network, IEEE Trans Ind. Inf. 14 (9) (2018) 3956–3969, https://doi.org/10.1109/TII.2017.2783334.

[23] S.M. Ahsan, N. Gholizadeh, P. Musilek, Multi-agent systems in networked microgrids: reinforcement learning and strategic pricing mechanisms, Ren. Energy 254 (2025) 123678, https://doi.org/10.1016/J.RENENE.2025.123678.

[24] J. Zhang, Z. Liang, L. Guan, W. Lu, C. Jiang, X. Zeng, Distributed multiple time scales energy management strategy for microgrid cluster with electric vehicles participation, Electr. Power Syst. Res. 248 (2025) 111923, https://doi.org/10.1016/J.EPSR.2025.111923.

[25] M.A. Babaei, S. Hasanzadeh, H. Karimi, Cooperative energy scheduling of interconnected microgrid system considering renewable energy resources and electric vehicles, Electr. Power Syst. Res. 229 (2024) 110167, https://doi.org/10.1016/J.EPSR.2024.110167.

[26] J. Montoya, et al., Advanced Laboratory Testing Methods Using Real-Time Simulation and Hardware-In-The-Loop techniques: A survey of Smart Grid International Research Facility Network Activities, MDPI AG, 2020, https://doi.org/10.3390/en13123267.

[27] R. Sarrias-Mena, L.M. Fernández-Ramírez, C.A. García-Vázquez, F. Jurado, Electrolyzer models for hydrogen production from wind energy systems, Int J Hydrog. Energy 40 (7) (2015) 2927–2938, https://doi.org/10.1016/J.IJHYDENE.2014.12.125.

[28] M.M. Rashid, M.N. Morshedul Haque, T. Akhtar, M.S. Miah, Simulink model of controlling fuel cell powered direct current motor with comparative performance analysis, in: Proceedings of the 4th International Conference on Communication and Electronics Systems, ICCES 2019, 2019, pp. 1631–1637, https://doi.org/10.1109/ICCES45898.2019.9002577.

[29] N.M. Souleman, O. Tremblay, L.A. Dessaint, A generic fuel cell model for the simulation of fuel cell vehicles, in: 5th IEEE Vehicle Power and Propulsion Conference, VPPC '09, 2009, pp. 1722–1729, https://doi.org/10.1109/VPPC.2009.5289692.

[30] R. Jun, W. Kai, L. Liwei, Characteristics analysis of ultracapacitor-battery hybrid energy storage system, in: 2017 Chinese Automation Congress, 2018, https://doi.org/10.1109/CAC.2017.8243796.

[31] M.A. Hasan, S.K. Parida, An overview of solar photovoltaic panel modeling based on analytical and experimental viewpoint, Renew. Sustain. Energy Rev. 60 (2016) 75–83, https://doi.org/10.1016/J.RSER.2016.01.087.

[32] O. Tremblay, L.A. Dessaint, A.I. Dekkiche, A generic battery model for the dynamic simulation of hybrid electric vehicles, in: VPPC 2007 - Proceedings of the 2007 IEEE Vehicle Power and Propulsion Conference, 2007, pp. 284–289, https://doi.org/10.1109/VPPC.2007.4544139.

[33] Modbus Master - OPAL-RT - Communication Protocol, OPAL-RT TECHNOLOGIES Inc, 2022. Accessed: Nov. 05, 2024 [Online].. Available, https://www.opal-rt.com/software-communication-protocols/modbus-master/.

[34] IEEE Guide for Smart Grid Interoperability of Energy Technology and Information Technology Operation with the Electric Power System (EPS), End-Use Applications, and Loads, 2011, https://doi.org/10.1109/IEEESTD.2011.6018239.